Imaging brain amyloid deposition using grating-based differential phase contrast tomography

B.R. Pinzer [a,1], M. Cacquevel [b,1], P. Modregger [a,c], S.A. McDonald [d,2], J.C. Bensadoun [b], T. Thuering [a,d], P. Aebischer [b], M. Stampanoni [a,d,*]

[a] *Swiss Light Source, Paul Scherrer Institut (PSI), 5232, Villigen-PSI, Switzerland*
[b] *École Polytechnique Fédérale de Lausanne (EPFL), Brain Mind Institute, 1015, Lausanne, Switzerland*
[c] *Faculty of Biology and Medicine, University of Lausanne, 1015, Lausanne, Switzerland*
[d] *Institute of Biomedical Engineering, ETH Zurich, 8092, Zurich, Switzerland*

ARTICLE INFO

ABSTRACT

One of the core pathological features of Alzheimer's disease (AD) is the accumulation of amyloid plaques in the brain. Current efforts of medical imaging research aim at visualizing amyloid plaques in living patients in order to evaluate the progression of the pathology, but also to facilitate the diagnosis of AD at the prodromal stage. In this study, we evaluated the capabilities of a new experimental imaging setup to image amyloid plaques in the brain of a transgenic mouse model of Alzheimer's disease. This imaging setup relies on a grating interferometer at a synchrotron X-ray source to measure the differential phase contrast between brain tissue and amyloid plaques. It provides high-resolution images with a large field of view, making it possible to scan an entire mouse brain. Here, we showed that this setup yields sufficient contrast to detect amyloid plaques and to quantify automatically several important structural parameters, such as their size and their regional density in 3D, on the scale of a whole mouse brain. Whilst future developments are required to apply this technique *in vivo*, this grating-based setup already gives the possibility to perform powerful studies aiming at quantifying the amyloid pathology in mouse models of AD and might accelerate the evaluation of anti-amyloid compounds. In addition, this technique may also facilitate the development of other amyloid imaging methods such as positron emission tomography (PET) by providing convenient high-resolution 3D data of the plaque distribution for multimodal comparison.

© 2012 Elsevier Inc. All rights reserved.

Introduction

Alzheimer's disease (AD) is the most common form of dementia in the elderly (Reitz et al., 2011). It is characterized by an insidious onset and a progressive decline of cognitive functions associated with predominant memory impairment. AD diagnosis is based mostly on the neuropsychological evaluation of the patient, which is always confirmed by the *post mortem* examination of the brain (McKhann et al., 1984). Indeed, two histopathological features characterize an AD brain: the amyloid plaques (AP) and the neurofibrillary tangles (NFTs). These lesions are formed of proteinaceous aggregates, which can be detected throughout the brain in the extracellular and the intracellular compartment, respectively. They appear early in the course of the disease several years before the occurrence of the first symptoms, and they spread to the temporo-parietal neocortex and subcortical nuclei following a typical pattern as the disease progresses (Braak and Braak, 1991; Delacourte et al., 1999; Thal et al., 2002). Therefore, detecting these two AD hallmarks through imaging techniques performed on the living patient is of major interest not only for diagnosis, but also for the evaluation of AD-modifying drugs.

Until recently, imaging techniques have been used mainly to exclude other causes of dementia (Petrella et al., 2003). However, significant technical progresses have been made, which now allow clinicians to use both structural and functional imaging to diagnose AD positively (Frisoni et al., 2010; Nordberg et al., 2010). New criteria for AD, mostly based on brain imaging, have even been proposed (Dubois et al., 2007, 2010; Reitz et al., 2011; Sperling et al., 2011). Among the recent progresses, the development of new tracers for Positron Emission Tomography (PET) dedicated to AD diagnosis like the flutemetamol, florbetapir, and florbetaben (Herholz and Ebmeier, 2011) offers the possibility to visualize the global averaged distribution of amyloid plaques in the brains of living patients. Unfortunately, this technique has a millimeter-range resolution and does not allow for the

detection of amyloid deposits at a single-plaque level, which might result in a limited sensitivity, especially at the onset of the disease.

Imaging amyloid plaques at a single-plaque resolution remains a technical challenge because of their small size. They are spherical extracellular aggregates that range from <10 μm to >120 μm in diameter, depending on the brain region where they are observed with a major proportion of plaques around 10–40 μm in humans (Armstrong et al., 1995; Delaère et al., 1991). They are heterogeneous in shape and composition, and their morphology varies from diffuse (amorphous material) to focal deposits (dense aggregates), a typical plaque combining a dense core and a corona of fibrils (Dickson and Vickers, 2001; Wisniewski et al., 1989). Among current imaging techniques that could be used to detect amyloid plaques at a single-plaque resolution, Magnetic Resonance Imaging (MRI) has shown promising results. Several reports have indicated that microMRI devices are able to detect single amyloid plaques in the brain of transgenic mouse models of Alzheimer's disease, both *ex vivo* and *in vivo* (Braakman et al., 2006; Dhenain et al., 2009; Jack et al., 2005; Petiet et al., 2011; Vanhoutte et al., 2005; Wadghiri et al., 2003; Wengenack et al., 2011; Yang et al., 2011; Zhang et al., 2004) and in human brain tissue (Benveniste et al., 1999) (See Braakman et al., 2009 for an extensive review). However, this technique is currently limited by its relatively low spatial resolution when compared to the mean plaque size measured in human brains. Although this parameter varies depending on the device, the MRI sequence, and the time of acquisition, so far only large amyloid deposits, which represent a small fraction of the total amyloid burden, could be detected and quantified by this technique in small animals. Below this limit, the specificity of the signal remains to be established even if abnormal radiologic features could be detected (Diaz-de-Grenu et al., 2011; van Rooden et al., 2009).

Another imaging technique that has been widely used for AD diagnosis is X-ray Computed Tomography (CT). Although MRI is now preferred to CT to assess macroscopic changes in AD patients – mainly because it is less invasive – a new set of experimental imaging techniques, also based on X-rays, is currently under development. In contrast to conventional absorption-based CT, these methods rely on sensing the phase shift induced by the interaction of X-rays with matter. The result is a considerable improvement of contrast in soft tissue (Zhou and Brahme, 2008). These methods include propagation-based methods (Cloetens et al., 1999; Groso et al., 2006), analyzer-based methods like diffraction enhanced imaging (DEI) (Chapman et al., 1997) and interferometric methods using a crystal (Bonse and Hart, 1965; Momose, 1995) or a grating interferometer (McDonald et al., 2009; Weitkamp et al., 2005). Among them, two setups have been shown to image amyloid plaques *ex vivo* in mouse models of AD (Connor et al., 2009; Noda-Saita et al., 2006). The setup presented here – based on a grating interferometer – provides higher quality images, giving the possibility to visualize both anatomical features and individual amyloid plaques at a micrometer resolution in the entire brain of a transgenic mouse model of AD, without using any contrast agents and in a nondestructive manner. With the high-quality images obtained from these scans, automated quantification of plaque features like size and density over the entire brain was possible. The measurement technique together with automated segmentation render large cross-sectional studies feasible and will facilitate multimodal comparison with other imaging techniques. The ability of this setup to further increase the resolution of images in selected areas by performing local tomography (McDonald et al., 2009) opens also new possibilities, such as visualizing the morphology of amyloid plaques in large brain areas.

Materials and methods

Animals and brain processing

The 5xFAD mouse line was generated in the laboratory of Dr Robert Vassar at Northwestern University, Chicago (Oakley et al., 2006) and was transferred to the École Polytechnique Fédérale de Lausanne (EPFL) in 2009 from Jackson Laboratories, US (Stock number: 006554). This transgenic line over-expresses both the amyloid precursor protein gene (*APP*) and the presenilin-1 gene (*PSEN1*), carrying familial AD mutations: APP K670N/M671L (Swedish), I716V (Florida) and V717I (London); PSEN1 M146L and L286V.

Animals were euthanized by intraperitoneal injection of pentobarbital (150 mg/kg) and transcardially perfused by cold phosphate buffered saline (PBS). Subsequently, the brains were harvested, fixed with 4% paraformaldehyde in PBS for a week at 4 °C and stored in sterile PBS until further processing. The brain samples were brought to the Swiss Light Source in order to perform the tomographic scanning, and then transferred back to EPFL for histology. All procedures were approved by the Committee on Animal Experimentation for the canton of Vaud, Switzerland, in accordance with Swiss Federal Laws on Animal Welfare and the European Community Council directive (86/609/EEC) for the care and use of laboratory animals.

Histology

In order to avoid tissue distortion during the histological process, thick brain sections (400 μm) were prepared using a vibratome (Leica VT1200S). Brain sections were next stained by Thioflavin S (Sigma-Aldrich) according to the following procedure. Free-floating sections were incubated in a solution of Thioflavin S 0.01% (w:v) in ethanol 50% for 8 min at room temperature under low agitation and were next washed in two baths of ethanol 50% (2 × 5 min) and two baths of PBS (2 × 10 min). Sections were next mounted in glycerol 80% using secure-sealed spacers (Invitrogen).

Fluorescence microscopy

Multi-photon fluorescence imaging

Thick brain sections stained by Thioflavin S were acquired on a LEICA SP5 Multi-photon microscope (Leica Microsystems, Germany) at the EPFL bioimaging and optics facility (http://biop.epfl.ch). A motorized platform was used to scan the whole sections at 8000 Hz with a Plan-Apochromat 10×/0.40 glycerine immersion objective (Leica #11506293). Excitation was performed at 800 nm and external Non Descanned Detectors (NDD) were used to capture the emitted fluorescence between 500 nm to 650 nm. 130 stacks covering the whole section were acquired at a frame resolution of 512 × 512 pixels every 4 μm (final voxel size in xyz: 2 μm × 2 μm × 4 μm), and were stitched together using the Leica Application Suite Software.

Processing of fluorescence images

The fluorescence images did not require any further normalization step. For noise reduction, a Lagrangian-of-Gaussian (LoG) filter, also known as Mexican-hat filter, was applied. This type of convolution filter is well known to serve as a detector for spherical particles in background noise (Sage et al., 2005). In our case, an isotropic Gaussian σ filter size of 2^3 voxels gave the best results. The LoG filter was applied to the image stack in 3D to emphasize the spherical plaques embedded in background noise.

Differential phase contrast (DPC) tomography

DPC image acquisition

In X-ray optics, the interaction of X-rays with typical materials is encoded in the material's index of refraction $n = 1 - \delta + i\beta$, where δ is the decrement of the real part of the refractive index (responsible for the phase shift) while the imaginary part β describes the absorption properties of the tissue. Since biological tissue (e.g. brain matter) consists mainly of light elements like water and hydrocarbons, there is negligible absorption contrast, and thus conventional (absorption-based) X-ray tomography is not suited to distinguish anatomical or

pathological features in soft tissue. However, at diagnostically relevant photon energies (between 10 and 130 keV), the decrement of the real part of the refractive index in soft tissue is three orders of magnitude larger than the absorption coefficient. Therefore, a better contrast is obtained if an adequate phase-sensitive measurement technique is used (Momose and Fukuda, 1995).

To measure the phase shift impressed on the wave front when it passes through the sample, we used a grating interferometer (GI) together with a phase-stepping protocol as described previously (McDonald et al., 2009; Weitkamp et al., 2005). The GI allows measurement of the very small refraction angles (on the order of submicro-radians, Modregger et al., 2011) with respect to the undisturbed wave, by determining the refraction-induced lateral displacement of an interference pattern. Because the length scale of this displacement is much smaller than one pixel, the phase-stepping approach virtually decouples the pixel size of the camera from the measurement of the refractive shift of the interference pattern, which can be viewed as an implementation of a "ruler". To produce this ruler, a π-shifting phase grating is used to imprint a periodic intensity variation on the beam. Refraction by the sample leads to a lateral deflection of the interference pattern by a small fraction of its period, which can be detected by scanning the interference pattern with an absorption mask of the same periodicity. The resulting bright–dark pattern in each pixel, called a phase stepping curve, allows for measuring the displacement and thus the refraction angle in every pixel of the detector. For an in-depth review of the measurement technique, the reader is referred to McDonald et al. (2009).

The presented data sets were obtained at the TOMCAT beamline of the Swiss Light Source (Stampanoni et al., 2007) (see also supporting information Fig. S1), at a photon energy of 25 keV, using 8 phase-steps distributed over 2 periods of the phase stepping curve. The relative bandwidth of the beam was about 10^{-2}, a typical value for a multilayer monochromator. The distance between the two gratings was set to the third fractional Talbot distance, i.e. 121 mm, as shown in the picture of the setup provided as supplementary Fig. S1. The absorption (analyzer) grating G2 had a pitch of 2 μm, which determined the design pitch for the phase grating G1 to be 3.981 μm, taking the magnification effect by the diverging beam and the source-to-G1 distance of 25 m into account. The detector directly behind the analyzer grating was realized by a CCD camera with 7.4 μm pixel size (PCO2000), coupled to a LuAG:Ce scintillator (350 μm thickness) via a 1:1 optics. When referring to local tomography later in the text, only the detector system was modified as follows: instead of the 1:1 optics, a 4× magnification objective was used and the photons were captured by binning 4 pixels (binning factor of 2 in each direction). Therefore, the pixel size was 3.7 μm, with a width of the field of view of 3.8 mm, the height still being limited by the height of the beam (about 3 mm).

For the comparison with histology, the brain was scanned with an exposure time of 300 ms, and the tomographic reconstruction was based on 2000 projections covering 180° of rotation. For the study of the kinetics of amyloid deposition in 5xFAD mice, where the brains of 11 animals were scanned, the combination of exposure time vs. number of projections was 240 ms vs. 2400 projections. Both parameter sets resulted in a total exposure time of approximately 80 min. An order-of-magnitude estimate of the rate of dose deposition in the sample can be obtained by assuming the absorption properties of water for the brain, which is suggested by the lack of absorption contrast between brain and water (see supporting information, Fig. S3). Based on a photon flux of $7.8 \times 10^{10} \, s^{-1} \, mm^{-2}$ impinging on the sample and an approximate absorption of 22% (that of a 10 mm water column illuminated with 25 keV photons), a dose rate of about 6.9 Gy/s is obtained, corresponding to a total volume-averaged dose of about 3×10^4 Gy. This dose would be lethal for a living animal; however, it is below the 10^6 Gy needed to induce significant structural changes (Kirz et al., 1995). Accordingly, we did not observe any morphological modifications on histological sections after the scan. This justifies the

relatively high number of phase steps as well as the large number of tomographic projections, which were chosen to optimize the signal-to-noise ratio, regardless of the deposited dose. The issue of dose reduction is addressed below in the discussion section.

Processing of DPC images

A general problem that can be traced back to monochromator vibrations is the inhomogeneous background within the slices and different offsets in gray values across slices. Therefore, as a key step for any further automated evaluation of the data, a normalization procedure in the sinogram space was developed. The principle of this filter is to normalize the sinogram of each slice by subtracting an azimuthally blurred version of itself. This procedure was inspired by the observation that the variations of background gray level had the form of circular sectors, varying with azimuth angle but not very much with the radius. Azimuthal blurring was achieved by applying a 1D Gaussian kernel filter with a large sigma of 100 pixels and a support of 600 pixels, only along the angular axis of the sinogram. The particular width of the Gaussian was determined heuristically — a balance between erasing small features (for small sigma) and increasing edge-enhancement artifacts (for large sigma). The sinograms were periodically continued to projection angles φ<0 and φ>180° before filtering, in order to avoid artifacts at the boundary pixels. Note that this filtering procedure emphasizes the small-scale features like amyloid plaques, but blurs features with a low spatial frequency (e.g. anatomical features) and introduces edge-enhancement artifacts around the outer surface of the brain (e.g. Fig. 4). After this normalization step, all slices had the same base gray level. Finally, noise reduction was achieved by applying a 3D LoG filter as described in the Processing of fluorescence images section.

Registration of DPC data with histological images

The comparison of CT images to histological images required a semi-automatic registration procedure. First, the DPC data set was rotated in 3D (bicubic interpolation, implemented with ImageJ) to place the antero-posterior axis of the brain perpendicularly to the coronal plane of the histological images. This was done interactively, guided by anatomical features and the small lesion that was accidentally produced during the extraction of the brain. Second, to register a slice of the fluorescence images with the corresponding CT slice, a landmark based rigid registration was first performed (Thevenaz et al., 1998), followed by an elastic registration based on vector-spline regularization (Sorzano et al., 2005). The registration was based on the gray level images. Finally, for a direct object-by-object comparison, histogram based segmentation of the two images was carried out, with an automatically determined threshold according to the maximum entropy method (Kapur et al., 1985).

Quantitative analysis

Depending on the quality of the extracted brain, the two neocortices or only one cortex per animal were segmented in order to avoid possible bias on the quantification procedure. Cerebral cortices were manually delineated using a Wacom Cintiq 12WX tablet according to the Allen mouse brain atlas (www.brain-map.org) and the Paxinos atlas (Paxinos and Franklin, 2001) on subsequent 2D coronal slices using the segmentation-editor plugin for ImageJ (http://www.neurofly.de/). Each cortex was segmented slice-by-slice at the front and the back of the structure and approximately every 10th slice in the central part of the brain and interpolated with the plugin. Within the resulting 3D ROI, an automatic threshold segmentation was carried out slicewise according to the maximum entropy method (Kapur et al., 1985). Since this automatic threshold was fluctuating between different slices, a mean of all slices was finally applied to the entire data set. The variation between different slices provides a measure of the uncertainty for the threshold determination. Since quantitative parameters derived from the segmented plaque data

are sensitive to the chosen threshold, this uncertainty value translates into an error estimate of the quantitative parameters. The spatial resolution of an optical system is essential for the visualization of small objects, especially if quantitative conclusions are drawn from it. Therefore, we made a rigorous model-independent assessment of the resolution by determining the highest spatial frequency component that is still distinguishable from the baseline of the background noise (Poisson noise from counting statistics plus white readout noise) (Modregger et al., 2007). This highest frequency component is directly related to the minimal structure size present in the image by $x_{res} = 2\pi/k_{res}$. Objects below this limit were excluded from the quantitative analysis. The size distribution of amyloid plaques was determined by counting the volume of individual, unconnected objects and assigning a diameter to each object that corresponds to an equivalent sphere of the same volume. This underlying sphere model represents the shape of the plaques very well.

The amyloid plaque load, defined as the proportion of a brain area covered by amyloid plaques, was measured in the segmented neocortex both on the 3D volume and on 2D coronal sections along the antero-posterior axis in order to compare the data to previous histological studies (Jawhar et al., 2012; Katsouri and Georgopoulos, 2011). For the 2D analysis, four consecutive tomogram slices were merged in order to provide values corresponding to a virtual histological section thickness of 30 μm.

Results

Detection of amyloid plaques by DPC tomography

In order to show that DPC tomography is capable of detecting amyloid plaques in the brain, we used a new transgenic mouse model of Alzheimer's disease that presents a strong pathology. The 5xFAD transgenic line develops amyloid plaques as early as 2 months old in the frontal cortex and the subiculum. With aging, the pathology spreads to the whole neocortex and the hippocampus, as well as in sub-cortical regions, including the thalamus, the amygdala and the brain stem (Jawhar et al., 2012; Oakley et al., 2006). Importantly, this particular transgenic line presents amyloid plaques with a relatively small diameter (on the order of 20 μm), similar to those observed in humans (Armstrong et al., 1995).

We first performed a DPC scan on the posterior part of the brain of wild-type and 5xFAD mice at 13 months, an age at which abundant amyloid plaques are expected to be present in all cortical regions. The tomographic reconstruction of the real part of the refractive index is shown in Fig. 1. The setup provides a pixel size of $7.4 \times 7.4 \times 7.4\ \mu m^3$ for a field of view covering the entire coronal plane of the brain ($12.8 \times 12.8 \times 2\ mm^3$) and easily allows the visualization of the gross anatomy of the brain even on unprocessed DPC images. Cerebral cortices, hippocampi and ventricles are clearly visible in both wild type (Fig. 1A) and transgenic brains (Fig. 1B). Among other brain structures, the corpus callosum, the hippocampal layers, the mammillothalamic tracts and the fasciculus retroflexus, two bilateral fiber tracts that appear as round hypo-intense signals (Fig. 1A and B), are also easily visualized (See also supporting information, Fig. S2, for a more extensive description of several sections of a whole mouse brain). It is important to note that such a high contrast could not be achieved by absorption tomography, because the signal-to-noise ratio of this sample is extremely low, even with the high dose that was deposited here. For the interested reader, a direct comparison of absorption contrast vs. phase contrast is shown in the supplementary Fig. S3, for a slice of the same brain as in Fig. S2. The absorption image was reconstructed from the same raw data, implying the same dose. However, without the grating interferometer (and thus post-sample absorption by the analyzer grating), an absorption image with equal signal-to-noise ratio could have been recorded with half the dose. Despite this difference, the advantages of phase contrast imaging are obvious.

When comparing the wild type and the AD mouse brains, we observed small hyper-intense dots throughout the neocortex and the hippocampus, which were only detected in the AD mouse brain (compare Figs. 1A and D with Figs. 1B and E). The contrast of these hyper-intense dots was particularly high in the piriform cortex/amygdala region (Fig. 1E). In addition, the distribution of these hyper-intense dots and the one of amyloid plaques revealed by Thioflavin S were highly similar (Figs. 1C and F), suggesting that they were indeed amyloid deposits. These observations were consistently made in several transgenic brains. Occasionally, we were also able to visualize particularly intense dots in
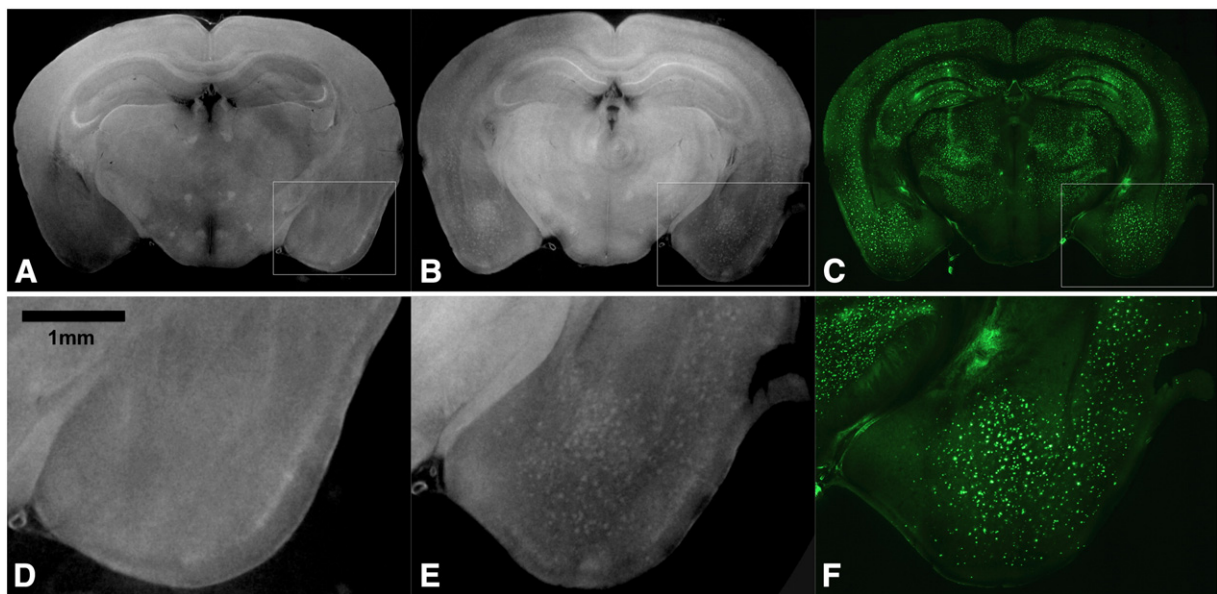

Fig. 1. Unfiltered DPC tomograms of a wild type (A, D) and a 5xFAD transgenic mouse brains (B, E) at 13 months. Brains were extracted and fixed in paraformaldehyde 4% for one week at 4 °C and were scanned by DPC tomography with an isotropic voxel size of 7.4 μm. The 5xFAD brain was next sliced at 400 μm and stained with Thioflavin S to reveal amyloid deposits (C, F). Lower panels (D, E, F) represent magnified regions of the whole brain images shown in the upper panels (A, B, C), at the level of the piriform cortex/amygdala region and at the same resolution.

the thalamus in a subset of AD mouse brains (Supporting information, Fig. S4). Such deposits have been previously described (Dhenain et al., 2009; Vanhoutte et al., 2005) and correspond to a particular subtype of amyloid deposit that contains a high proportion of calcium and iron.

In order to validate these observations, we directly compared the two sets of images (Fig. 2). The DPC volume was segmented as described in the Materials and methods section, and a 2D image from fluorescence microscopy was registered with the DPC tomogram. The different thickness of the slices was taken into account by averaging two subsequent fluorescence slices of 4 μm, in order to be close to the CT slice thickness of 7.4 μm. For a direct comparison, an animation that shows an overlay of 2D slices from both modalities is provided online (Supporting information, Video S1). Figs. 2A and B show the signals of the DPC scan and the fluorescence microscopy, respectively, before segmentation. The magnified insets compare the overlap of the detected structures, where the red color indicates a pixel-wise match of both techniques. Object-pixels that appear only in the DPC scan are colored in blue while object-pixels in the fluorescence image without correspondence in the DPC image are colored in green. A more global comparison within the region of interest, drawn as a black line in both images, shows that 75% of all detected objects in the DPC image (201 of 269) have a direct corresponding object in the fluorescence image (Fig. 2C). Inversely, 73% of all fluorescence objects (209 of 287) have a direct overlap with a DPC spot. The correspondence between the two signals was very good considering that the preliminary 3D alignment of the DPC data set was done manually. The slight distortion of the fluorescence image that was necessary to match the CT data indicates that even with thick histological sections, mechanical distortion cannot be avoided during the brain histological processing, highlighting the difficulties of comparing histological images to other imaging modalities.

Visualization of amyloid plaque morphology by local DPC tomography

In order to quantify smaller amyloid deposits, we next investigated the potential of the DPC setup to perform local tomography as previously described (Pfeiffer et al., 2008). This method allows imaging a sub-region of interest deep in the tissue at a high resolution (here: voxel size $3.7 \times 3.7 \times 3.7 \ \mu m^3$ for a field of view of $3.7 \times 3.7 \times 2.8 \ mm^3$). Based on the full-brain visualization, we selected and measured a brain sub-

region including parts of the striatum, the descendant part of the hippocampus, and the auditory/perirhinal cortex (Fig. 3A). At this resolution, and without post-processing of the images, the morphology of the hyper-intense dots that were previously observed on standard DPC images appeared clearly (Fig. 3B). Several spots were composed of a small and intense dense core surrounded by a corona made of weaker signal. Other spots were composed only of an intense and compact signal (Fig. 3C). The morphology of these spots is typical of the amyloid deposits that are observed in this AD transgenic mouse model as well as in humans (Duyckaerts et al., 2009) (compare to Fig. 3D).

Quantification of amyloid plaque burden

After confirming that we were indeed detecting amyloid plaques with DPC tomography, we next investigated the distribution of amyloid plaques in a whole transgenic mouse brain at 13 months. The rotation stage supporting the sample was translated along the anteroposterior axis of the brain for subsequent scans, in order to stitch together several fields of view. Six measurements were necessary to capture the whole brain. In order to highlight the amyloid-plaque signal and to suppress artifacts, the raw images were filtered as described in the Materials and methods section. Orthogonal views of the sinogram-normalized transgenic brain are presented in Fig. 4 (see also supporting information Video S2), showing the distribution of the amyloid deposits throughout the brain. To demonstrate the quantitative capabilities of this technique, we next focused on the right neocortex, which was manually drawn on slices based on the Allen mouse brain atlas. Within this region of interest, the signal to noise ratio was sufficient to perform a simple threshold segmentation of the amyloid deposits. The threshold was determined according to the maximum entropy criterion as described in the Materials and methods section. The standard deviation of the automatic threshold was 2.3% of the dynamic range of the gray levels.

The segmented collection of plaques contains objects of all sizes, including a size of only one voxel. Taking into account the finite resolution of the imaging system, it is not realistic to quantify the plaque size of amyloid plaques measuring only one voxel. Therefore, a Fourier analysis was applied to the raw images of the scan presented in Fig. 4 to determine the highest spatial frequency component that could be accurately measured in this data set. We obtained a spatial resolution
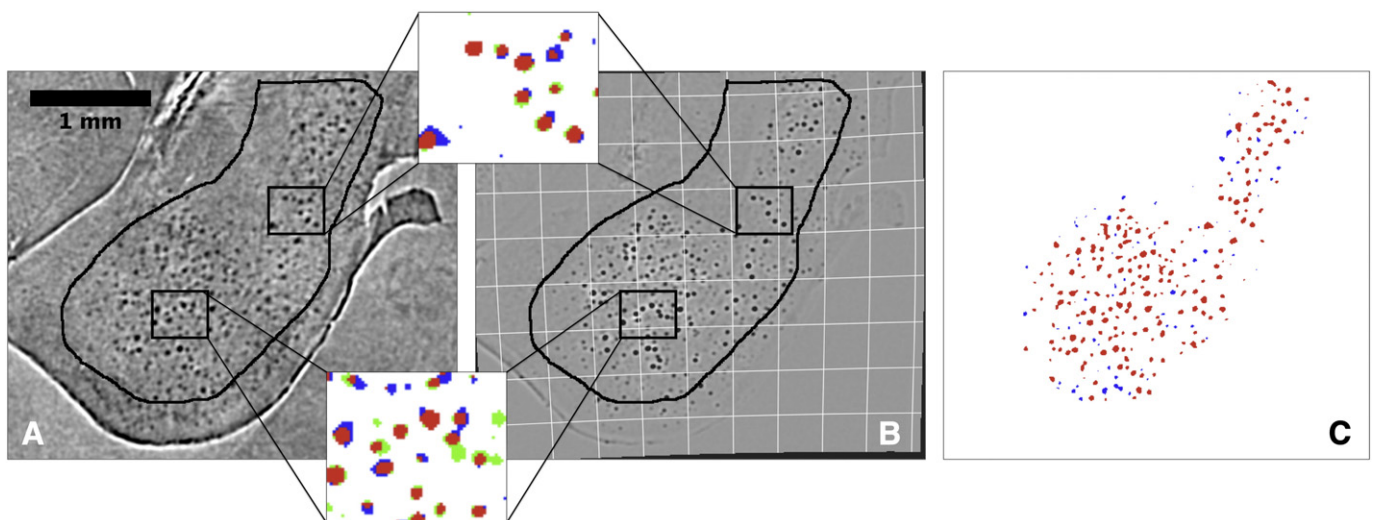

Fig. 2. Automated overlapping of DPC tomography and histology images from a 5xFAD transgenic mouse brain at 13 months old. DPC images were tilt-corrected in 3D, filtered (A) and were compared to filtered histological images (B) at the level of the piriform cortex/amygdala region. The grid depicted in B highlights the deformation that has been applied to the fluorescent image to correct artifactual stretching during histological processing. The small insets show details of the overlap of the segmented images. DPC deposits are indicated in blue and histology deposits in green. Overlap is indicated in red. C — Overview of the overlap between both signals at a larger scale. The image depicts the segmented objects in the DPC image, with red particles having a direct corresponding particle in the fluorescence image and blue particles lacking an overlapping partner in the fluorescence image.
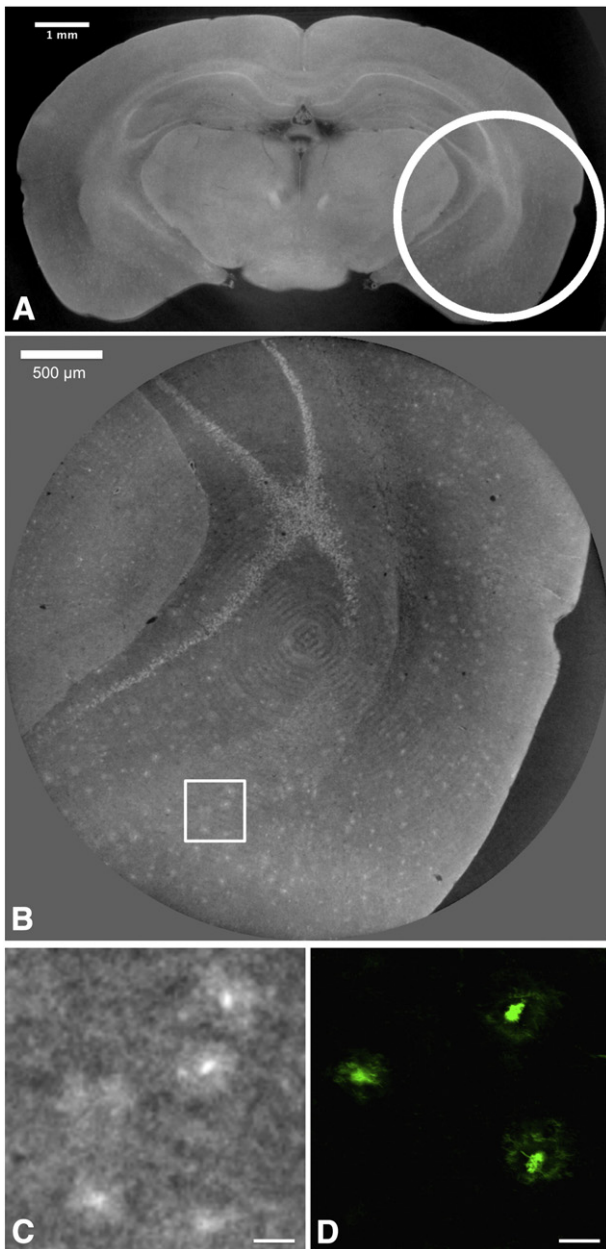
Fig. 3. High-resolution DPC tomogram of a 5xFAD mouse brain at 13 months old. A — Low-resolution scan of the whole brain showing the position of the brain region (entorhinal and perirhinal cortex/hippocampus) that was scanned at high resolution ($3.7 \times 3.7 \times 3.7\ \mu m^3$) (B). C — Detail of the high resolution scan. The structure of amyloid deposits, consisting of a dense core surrounded by diffuse material, is clearly visible and comparable to the one revealed by Thioflavin S staining on similar brain sections (D).

plaques in the cortical region shown in Fig. 4 and in particular in the Video S3 was 16,561 (18,588 without any size restriction). When the threshold was increased by one standard deviation as explained above, the total number of particles was decreased by 4110 (-24.8%). When the threshold was decreased by one standard deviation, the total number of particles increased by 8826 ($+53.3\%$). However, the visual inspection of the segmentation results clearly shows that these limits were worst-case scenarios and that a human operator would not choose such a threshold. These figures describe a possible systematic error, which must be distinguished from the repeatability of quantification for different data sets. For data acquired from different animals and processed according to the same protocol, it is shown below that the repeatability is better, meaning that relative changes between different data sets can be reliably detected.

The mean plaque size was a more robust parameter. For the same threshold variations as described above, the mean plaque diameter dropped from 36.3 to 34.0 μm (-6.3%) when increasing the threshold and increased to 38.0 μm ($+4.8\%$) when decreasing the threshold. These values were higher than the 20 μm of mean diameter reported by (Oakley et al., 2006), although in their study, no systematic quantification was performed. In addition, the exclusion of small plaques from this systematic analysis leads to an overestimation of these values. To confirm this hypothesis, the mean plaque size was evaluated in the high-resolution volume described above in Fig. 3. At this resolution, an automatic thresholding was not possible due to the complexity of the structure. Therefore, a manual threshold was applied visually (see supporting information Fig. S5). Two thresholds were compared, one considering only the dense core of amyloid plaques, the other considering both the core and the surrounding corona (Figs. S5A and B). Objects smaller than 3 voxels were excluded from the analyses because the spatial resolution was found to be close to 3 pixels. For the first threshold (plaque core), the distribution of amyloid plaque size was close to the quantification precision limit giving a mean plaque diameter of 13.1 μm (Fig. S5C). For the second threshold (plaque core and corona), the size distribution was similar to the one measured above in the whole neocortex, but with a significant fraction of smaller amyloid plaques (<20 μm), resulting in a mean plaque size of 27 μm. On the one hand, these data suggest that some plaques are too small to be reliably quantified with the larger voxel size of 7.4 μm. In that case, the lower resolution of the overview scan could lead to a smearing out of smaller plaques, which would mean that the plaques are detected but their size can not be precisely measured. Once a plaque would be so small as to completely fit within one voxel, the averaging of the differential phase signal over one detector pixel would lead in general to a zero signal, and thus very small objects could be missed. On the other hand, these data also indicate that the automatic segmentation of amyloid plaques that are larger than 20 μm is robust and takes into account the less compact material of the corona in amyloid plaques.

Finally, we explored the repeatability of the method in several 5xFAD animals at different ages from 12 to 70 weeks. Hyper-intense spots were detected as early as 12 weeks in several brain regions, mainly in the subiculum, but also in the neocortex, in the amygdala, and in different nuclei of the brain stem, such as the magnocellular part of the red nucleus, the oculomotor nucleus and the motor trigeminal nucleus. Although no systematic comparison with histology was performed in these sub-cortical brain regions, the morphology and the localization of the spots suggest they are indeed amyloid plaques. In addition, this observation suggests that DPC-imaging with a grating interferometer is capable of detecting amyloid plaques even in young animals whatever the state of amyloid plaque maturation. The visual inspection of the different brains confirmed the age-dependent accumulation of the amyloid pathology in the neocortex and in other brain regions like the amygdala (Fig. 5A). A systematic evaluation of amyloid plaque content was next performed for each brain according to the method described above. Fig. 5B presents three representative
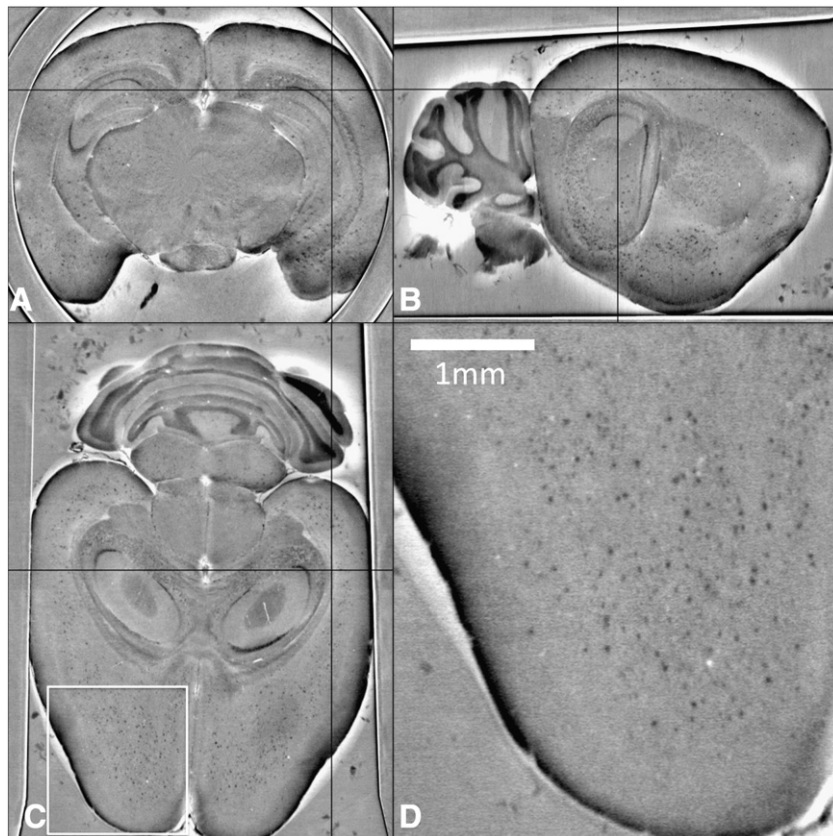
of 3 pixels, corresponding to 22 μm. For objects below this limit, plaques might appear larger than they are in reality, even if they are visually detectable on the images. To reduce the impact of noise on the quantitative evaluation, plaques measuring less than 4 voxels were not considered (See supporting information, Video S3, for a 3D animation of the plaque load distribution in the cortex under this restriction).

Two important structural parameters were quantified in the right neocortex: the density of plaques and their size distribution. The density of plaques (plaques/mm^3) was sensitive to small variations of the threshold. Even when carefully ignoring possible noise by focusing on plaques larger than 3 voxels, a variation in threshold yielded a significant change in the plaque number. For example, the total number of

Fig. 4. Overview of amyloid deposition in a 5xFAD transgenic mouse brain at 13 months old. A, B, C — Orthogonal views of a DPC tomogram with an isotropic voxel size of 7.4 μm that was post-processed to emphasize the amyloid deposition as described in the Materials and methods section. A sagittal stack of this brain is also available in Video S2. D — Detail of the horizontal view (C) at the level of the right frontal neocortex and at the same resolution.

data sets at different ages showing the progressive accumulation of amyloid plaques in the neocortex with age. For each brain, the amyloid plaque number and size were determined and summarized in Table 1 (See also supplementary Table S1 for complete data). In addition, an average plaque load corresponding to the proportion of the segmented brain region covered by amyloid plaques was also calculated for each neocortex, according to the Quantitative analysis section. This parameter was calculated from the 3D data set and from virtual 2D sections in order to facilitate comparison with previous reports. As shown in supplementary Fig. S6, the plaque load varies along the antero-posterior position. Therefore, the frontal and caudal regions were excluded from the analysis in order to provide more consistent data. The mean plaque load for each neocortex is represented in Fig. 6A. Both the plaque load and the number of amyloid plaques were increased with age (Supplementary Table S1). As shown in Fig. 6B, the amyloid plaque diameter also varies with age. Larger plaques were more frequent at later stages. Although intuitive, this data is of major importance for all methods aiming at visualizing single amyloid plaques. Indeed, it suggests that they will be more difficult to detect at early stages of amyloid deposition.

Discussion

DPC tomography overcomes several limitations of the classical, absorption-based CT-scan. In contrast to a traditional CT-scan, DPC tomography measures the refraction angle, i.e. the gradient of the local phase shift of the transmitted X-rays that is caused by their interaction with the tissue. DPC tomography thus takes advantage of a different contrast modality as compared to traditional (absorption) CT, resulting in a considerable improvement of the image contrast

in soft tissues (see supplementary Fig. S3 for a comparison of absorption and phase contrast).

Here, we applied DPC tomography to brain imaging and proved that this technique can be used to image one of the pathological hallmarks of Alzheimer's disease in brains: the amyloid plaque. In this study, we were not only able to visualize the anatomy of a mouse brain in more physiological conditions than previously reported (McDonald et al., 2009), but also to detect amyloid plaques in the brain of a transgenic mouse model of Alzheimer's disease. The resolution of the technique allowed us to visualize deposits as small as 10 μm in the whole brain, and to perform an automatic quantification of their number, size and density in defined ROIs.

In contrast to previous studies aiming at visualizing and quantifying amyloid plaques in transgenic mouse models of Alzheimer's disease by using a phase-contrast approach, the major advantage of the approach described in this report is the quality of the images that it generates. The setup provides high spatial resolution images with a voxel size of $7.4 \times 7.4 \times 7.4$ or $3.7 \times 3.7 \times 3.7 \ \mu m^3$ for standard or local tomography, respectively. With such a resolution, it was possible to detect the vast majority of amyloid plaques as well as to visualize their morphology without using any contrast agent. In comparison to the method described by Connor and colleagues (Connor et al., 2009), which is based on DEI and provides images with similar pixel size ($9 \times 9 \times 9 \ \mu m^3$), the setup presented here generates highly contrasted images, giving the possibility to assess amyloid plaque features by a simple threshold segmentation. In contrast to Noda-Saita and colleagues (Noda-Saita et al., 2006), who have used a Bonse-Hart interferometer to capture plaque-signals (voxel size: $18 \times 18 \times 18 \ \mu m^3$) and have performed an interactive threshold-segmentation of amyloid plaques, the quality of the images generated by our setup allowed us to segment the amyloid
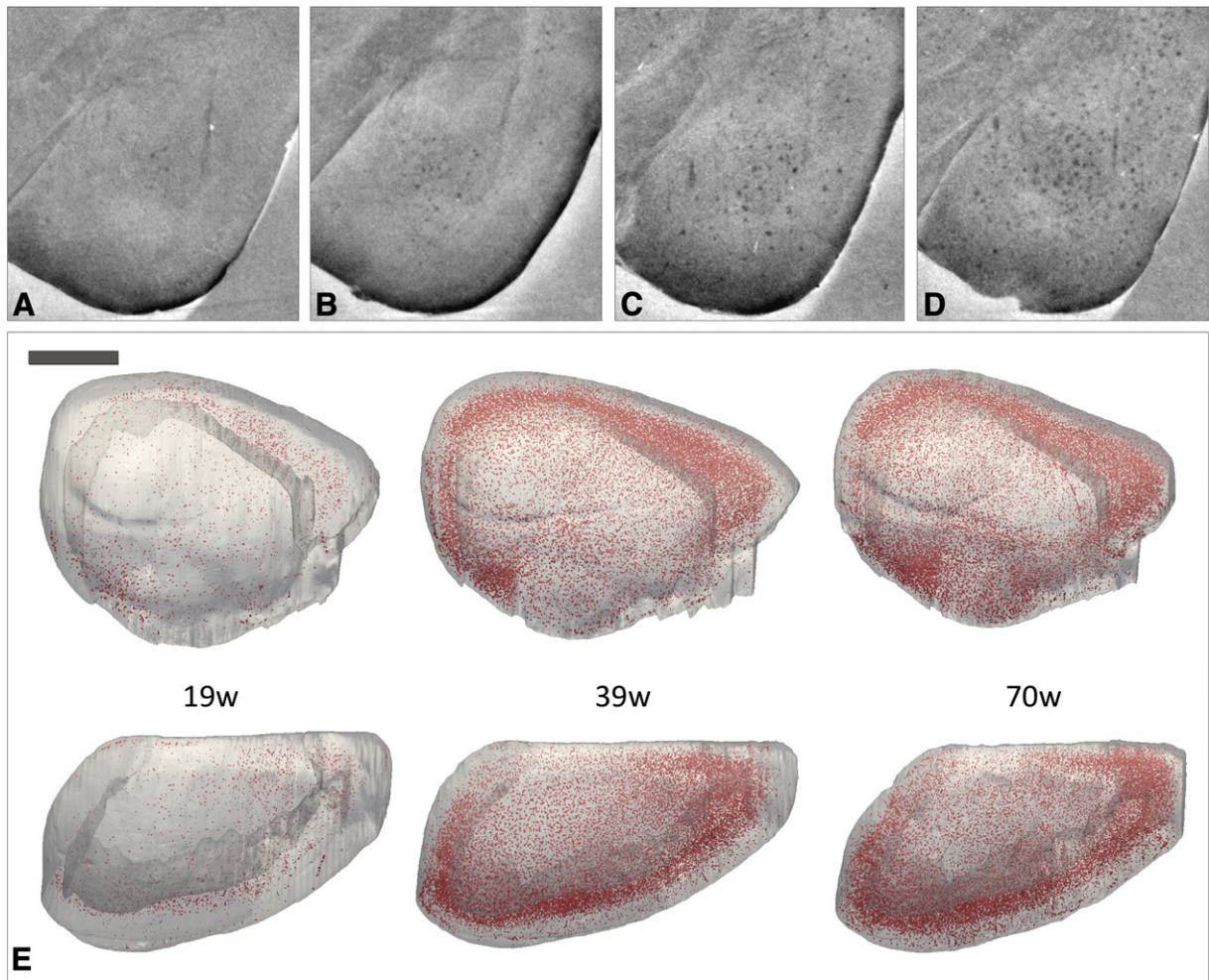
Fig. 5. Kinetics of brain amyloid deposition in 5xFAD mice. A–D — Representative DPC scans of 5xFAD mouse brains at the level of amygdala at 12 (A), 19 (B), 39 (C), 70 weeks of age (D). E — Representative 3D views of the right neocortex of 5xFAD mice at different ages (upper panel: lateral view; lower panel: top view) showing the distribution of amyloid plaques (in red) segmented as described in the Quantitative analysis section.

plaque signal automatically. This is a significant step since all of the parameters that were measured are sensitive to the chosen threshold, in particular the number of plaques. Indeed, although it is reasonable to perform a manual thresholding of plaque signal in a small ROI because a trained operator can verify the segmentation visually, this strategy becomes extremely time-consuming and less accurate when assessing amyloid plaque load in large ROIs, such as in the whole mouse neocortex for example. In addition, a manual segmentation does not allow one to assess the influence of the threshold on the quantification. On the contrary, the method presented in this report provides an automatic quantification of amyloid plaques and an error estimate of the measurement that is important when absolute numbers are considered, and not only relative differences between samples.

An important feature of amyloid plaques is their size. Imaging amyloid plaques at two different resolutions has revealed the significance of spatial resolution for plaque size determination. Here, we show that we

Table 1
Evaluation of amyloid plaque deposition in 5xFAD mouse neocortex.

	n	Vol. ROI[a]	Number of plaques[b]	Mean plaque diameter[c]	Plaque LOAD 3D[d]	Plaque LOAD 2D[e]
12 weeks	1	68.51	2214	24.15	0.08	0.1
19 weeks	4	64.94 ± 3.01	7535 ± 5180	25.73 ± 1.51	0.16 ± 0.13	0.35 ± 0.28
39 weeks	3	65.79 ± 1.22	37154 ± 6604	31.49 ± 0.53	1.30 ± 0.16	2.60 ± 0.30
70 weeks	3	61.58 ± 2.69	48610 ± 11085	31.19 ± 1.15	1.75 ± 0.37	3.54 ± 0.66
Age effect *p* value[f]		*ns*	*0.024*	*0.038*	*0.018*	*0.018*

[a] Mean volume of the right neocortex ± SD (mm^3).
[b] Mean number of amyloid plaques in the right neocortex ≥ 3 voxels ± SD.
[c] Mean plaque diameter in μm ± SD.
[d] Mean volume of the right neocortex covered by amyloid plaques ± SD (in %).
[e] Mean area in the right neocortex covered by amyloid plaques determined on virtual 2D coronal sections (Thickness: 30 μm) (Mean ± SD in %).
[f] Kruskal–Wallis non-parametric test was performed on 19-, 39- and 70-week-old-animals to determine the effect of age on all the parameters. *ns*: non significant.
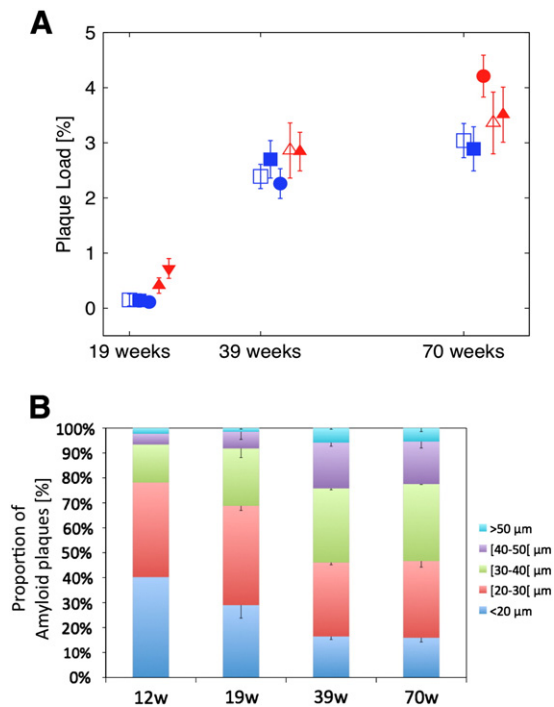
Fig. 6. Quantification and size distribution of amyloid deposits in the neocortex. Several brains between 12 and 70 weeks of age were scanned and segmented according to the method described in the Quantitative analysis section. Depending on the quality of the extracted brains, one or two neocortices were segmented per animal for the quantification. A — Quantification of amyloid plaque burden was performed in the neocortex on coronal 2D sections along the antero-posterior axis as described in the Quantitative analysis section. Data are represented for each segmented neocortex as Mean +/− SD of all the values calculated along the longitudinal axis (see also supplementary material S4 and Table S1 for the complete data). Each symbol represents a segmented region corresponding to the left (empty symbols) or right neocortex (filled symbols). Blue symbols correspond to males and red symbols to females. B — The diameter of each segmented amyloid plaque was determined for each animal on the whole segmented volume and is depicted by size classes from <20 μm to >50 μm. Data are represented relative to the total number of plaques at each age of analysis as Mean +/− SD. At 12 weeks of age, only one brain was scanned and is just shown for comparison (12 weeks, n = 1; 19 weeks, n = 4; 39 weeks, n = 3; 70 weeks, n = 3).

can accurately measure amyloid plaques larger than 20 μm in diameter over the entire brain, even though plaques are detectable below this limit. This limit falls to 10 μm when using local DPC tomography. Therefore, by using local DPC tomography, one can already measure the size distribution of the majority of plaques and even visualize plaque substructure.

In summary, we present the first imaging technique that produces images with a sufficient signal-to-noise ratio for automated segmentation of amyloid plaques and a resolution high enough to assess their size distribution. The segmentation routine used in the present study did not involve the intervention of a trained operator, and the threshold fluctuations naturally lead to an error estimate for the plaque parameters.

Currently, recording one complete tomogram at a voxel size of 7.4 μm requires 80 min, resulting in the deposition of roughly 3×10^4 Gy of total radiation dose. Such doses are not compatible with *in vivo* applications, and are a consequence of the high resolution of the measurements. A general relationship between dose and resolution for DPC is difficult to establish, because of the completely different noise properties of phase contrast images compared to classical absorption tomography (Koehler et al., 2011; Raupach and Flohr, 2011). In the latter case, the dose scales with the 4th power of the required resolution when the signal-to-noise ratio is kept constant (Bonse and Busch, 1996). The problem of 'mixed voxels', i.e. when an object occupies only part of a voxel, plays an even more important role in DPC imaging, since in the

extreme case where an object is completely contained in one pixel, the fringe phase value will average to zero within that pixel and the object would not be detected.

Nevertheless, several modifications in the method in order to decrease the time of exposure and therefore the dose received by the tissue are under development. For instance, in this work, we used a phase stepping approach with 8 phase steps to extract the refraction information. Therefore, the sample was exposed 8 times for one angular step. It has been shown recently that an alternative method with only two projections per angular step was possible (Zhu et al., 2010). This would decrease the exposure time by a factor of 4. Another line of research towards faster tomography is to use fast and more efficient detectors to reduce the exposure time of each single acquisition. Absorption tomography in the range of 1 s, with exposure times on the order of milliseconds, has been already demonstrated (Mokso et al., 2010). Other technical modifications such as improving the efficiency of the scintillator could also decrease the deposited dose on the specimen, but further investigations are necessary to determine the impact of these modifications on the imaging capacities of our setup. By far the most promising approach to reduce the dose would be to use higher X-ray energies (100 keV or higher). Higher energies could also possibly solve another issue specific to brain imaging, the significant interaction of X-ray radiation with the skull. The problem is that the high sensitivity of the setup required to detect minute differences in electron density within the brain is not compatible with the high phase contrast of the skull, which introduces severe phase wrapping artifacts. In addition, the strong absorption of the skull decreases the signal to noise ratio (Revol et al., 2010) inside the brain region to a level where interpretation becomes unfeasible. The major challenge for going to higher energies is the fabrication of reliable absorption gratings that block high energy photons. So far, this technique is not applicable to *in vivo* studies, but there is high potential to reduce the deposited dose from X-ray radiation.

In the meantime, this technique is already useful to the neuroscience community by facilitating the analysis of the amyloid plaque load in an AD transgenic mouse brain *ex vivo*. The relatively short measurement time together with the ease of sample preparation and segmentation allows for large studies with a statistically relevant number of samples. One possible application for this setup would be to facilitate the validation of new PET-scan biomarkers or other imaging methods aiming at visualizing amyloid plaques *in vivo*. Indeed, their validation requires a comparative histological study that involves time-consuming histological sectioning and staining of amyloid plaques as well as complex 2D/3D registration to compare both images. The setup presented here generates high-resolution isotropic 3D images of a whole mouse brain, on which the large majority of amyloid plaques can be detected and segmented automatically, facilitating multimodal comparison. Furthermore, the surrounding brain anatomical structures are clearly visible with this technique, allowing the fine segmentation of small regions of interest that could be helpful for generating precise masks for atlas based segmentation of brain structures in mice (Bae et al., 2009; Ma et al., 2008). Finally, the possibility to further increase the resolution in defined brain areas opens new possibilities to assess morphological changes in the small brain structures in pathological conditions.

Disclosure

The authors declare no conflict of interest.

Supplementary materials related to this article can be found online at doi:10.1016/j.neuroimage.2012.03.029.

Acknowledgments

References

Armstrong, R.A., Myers, D., Smith, C.U., 1995. What determines the size frequency distribution of beta-amyloid (A beta) deposits in Alzheimer's disease patients? Neurosci. Lett. 187, 13–16.

Bae, M.H., Pan, R., Wu, T., Badea, A., 2009. Automated segmentation of mouse brain images using extended MRF. Neuroimage 46, 717–725.

Benveniste, H., Einstein, G., Kim, K.R., Hulette, C., Johnson, G.A., 1999. Detection of neuritic plaques in Alzheimer's disease by magnetic resonance microscopy. Proc. Natl. Acad. Sci. U. S. A. 96, 14079–14084.

Bonse, U., Busch, F., 1996. X-ray computed microtomography (microCT) using synchrotron radiation (SR). Prog. Biophys. Mol. Biol. 65, 133–169.

Bonse, U., Hart, M., 1965. An X-ray interferometer. Appl. Phys. Lett. 6, 155-&.

Braak, H., Braak, E., 1991. Neuropathological stageing of Alzheimer-related changes. Acta Neuropathol. 82, 239–259.

Braakman, N., Matysik, J., van Duinen, S.G., Verbeek, F., Schliebs, R., de Groot, H.J., Alia, A., 2006. Longitudinal assessment of Alzheimer's beta-amyloid plaque development in transgenic mice monitored by in vivo magnetic resonance microimaging. J. Magn. Reson. Imaging 24, 530–536.

Braakman, N., van Buchem, M.A., Schliebs, R., de Groot, H.J., Alia, A., 2009. Recent advances in visualizing Alzheimer's plaques by magnetic resonance imaging. Curr. Med. Imaging Rev. 5, 2–9.

Chapman, D., Thomlinson, W., Johnston, R.E., Washburn, D., Pisano, E., Gmur, N., Zhong, Z., Menk, R., Arfelli, F., Sayers, D., 1997. Diffraction enhanced x-ray imaging. Phys. Med. Biol. 42, 2015–2025.

Cloetens, P., Ludwig, W., Baruchel, J., Van Dyck, D., Van Landuyt, J., Guigay, J.P., Schlenker, M., 1999. Holotomography: quantitative phase tomography with micrometer resolution using hard synchrotron radiation x rays. Appl. Phys. Lett. 75, 2912–2914.

Connor, D.M., Benveniste, H., Dilmanian, F.A., Kritzer, M.F., Miller, L.M., Zhong, Z., 2009. Computed tomography of amyloid plaques in a mouse model of Alzheimer's disease using diffraction enhanced imaging. Neuroimage 46, 908–914.

Delacourte, A., David, J.P., Sergeant, N., Buee, L., Wattez, A., Vermersch, P., Ghozali, F., Fallet-Bianco, C., Pasquier, F., Lebert, F., Petit, H., Di Menza, C., 1999. The biochemical pathway of neurofibrillary degeneration in aging and Alzheimer's disease. Neurology 52, 1158–1165.

Delaère, P., Duyckaerts, C., He, Y., Piette, F., Hauw, J.J., 1991. Subtypes and differential laminar distributions of beta A4 deposits in Alzheimer's disease: relationship with the intellectual status of 26 cases. Acta Neuropathol. 81, 328–335.

Dhenain, M., El Tannir El Tayara, N., Wu, T.-D., Guégan, M., Volk, A., Quintana, C., Delatour, B., 2009. Characterization of in vivo MRI detectable thalamic amyloid plaques from APP/PS1 mice. Neurobiol. Aging 30, 41–53.

Diaz-de-Grenu, L.Z., Acosta-Cabronero, J., Pereira, J.M., Pengas, G., Williams, G.B., Nestor, P.J., 2011. MRI detection of tissue pathology beyond atrophy in Alzheimer's disease: introducing T2-VBM. Neuroimage 56, 1946–1953.

Dickson, T.C., Vickers, J.C., 2001. The morphological phenotype of beta-amyloid plaques and associated neuritic changes in Alzheimer's disease. Neuroscience 105, 99–107.

Dubois, B., Feldman, H.H., Jacova, C., Dekosky, S.T., Barberger-Gateau, P., Cummings, J., Delacourte, A., Galasko, D., Gauthier, S., Jicha, G., Meguro, K., O'Brien, J., Pasquier, F., Robert, P., Rossor, M., Salloway, S., Stern, Y., Visser, P.J., Scheltens, P., 2007. Research criteria for the diagnosis of Alzheimer's disease: revising the NINCDS-ADRDA criteria. Lancet Neurol. 6, 734–746.

Dubois, B., Feldman, H.H., Jacova, C., Cummings, J.L., Dekosky, S.T., Barberger-Gateau, P., Delacourte, A., Frisoni, G., Fox, N.C., Galasko, D., Gauthier, S., Hampel, H., Jicha, G.A., Meguro, K., O'Brien, J., Pasquier, F., Robert, P., Rossor, M., Salloway, S., Sarazin, M., de Souza, L.C., Stern, Y., Visser, P.J., Scheltens, P., 2010. Revising the definition of Alzheimer's disease: a new lexicon. Lancet Neurol. 9, 1118–1127.

Duyckaerts, C., Delatour, B., Potier, M.C., 2009. Classification and basic pathology of Alzheimer disease. Acta Neuropathol. 118, 5–36.

Frisoni, G.B., Fox, N.C., Jack, J., Clifford, R., Scheltens, P., Thompson, P.M., 2010. The clinical use of structural MRI in Alzheimer disease. Nat. Rev. Neurol. 6, 67–77.

Groso, A., Abela, R., Stampanoni, M., 2006. Implementation of a fast method for high resolution phase contrast tomography. Opt. Express 14, 8103–8110.

Herholz, K., Ebmeier, K., 2011. Clinical amyloid imaging in Alzheimer's disease. Lancet Neurol. 10, 667–670.

Jack, J., Clifford, R., Wengenack, T.M., Reyes, D.A., Garwood, M., Curran, G.L., Borowski, B.J., Lin, J., Preboske, G.M., Holasek, S.S., Adriany, G., Poduslo, J.F., 2005. In vivo magnetic resonance microimaging of individual amyloid plaques in Alzheimer's transgenic mice. J. Neurosci. 25, 10041–10048.

Jawhar, S., Trawicka, A., Jenneckens, C., Bayer, T.A., Wirths, O., 2012. Motor deficits, neuron loss, and reduced anxiety coinciding with axonal degeneration and intraneuronal Abeta aggregation in the 5XFAD mouse model of Alzheimer's disease. Neurobiol. Aging 30, 196.e29–196.e40.

Kapur, J.N., Sahoo, P.K., Wong, A.K.C., 1985. A new method for gray-level picture thresholding using the entropy of the histogram. Comput. Vision Graph. Image Process. 29, 273–285.

Katsouri, L., Georgopoulos, S., 2011. Lack of LDL receptor enhances amyloid deposition and decreases glial response in an Alzheimer's disease mouse model. PLoS One 6, e21880.

Kirz, J., Jacobsen, C., Howells, M., 1995. Soft X-ray microscopes and their biological applications. Q. Rev. Biophys. 28, 33–130.

Koehler, T., Engel, K., Roessl, E., 2011. Noise properties of grating-based x-ray phase contrast computed tomography. Med. Phys. 38, S106–S116.

Ma, Y., Smith, D., Hof, P.R., Foerster, B., Hamilton, S., Blackband, S.J., Yu, M., Benveniste, H., 2008. In Vivo 3D digital atlas database of the adult C57BL/6J mouse brain by magnetic resonance microscopy. Front. Neuroanat. 2, 1.

McDonald, S.A., Marone, F., Hintermüller, C., Mikuljan, G., David, C., Pfeiffer, F., Stampanoni, M., 2009. Advanced phase-contrast imaging using a grating interferometer. J. Synchrotron Radiat. 16, 562–572.

McKhann, G., Drachman, D., Folstein, M., Katzman, R., Price, D., Stadlan, E.M., 1984. Clinical diagnosis of Alzheimer's disease: report of the NINCDS-ADRDA work group under the auspices of department of health and human services task force on Alzheimer's disease. Neurology 34, 939–944.

Modregger, P., Lubbert, D., Schafer, P., Kohler, R., 2007. Spatial resolution in Bragg-magnified X-ray images as determined by Fourier analysis. Phys. Status Solidi A 204, 2746–2752.

Modregger, P., Pinzer, B.R., Thuring, T., Rutishauser, S., David, C., Stampanoni, M., 2011. Sensitivity of X-ray grating interferometry. Opt. Express 19, 18324–18338.

Mokso, R., Marone, F., Stampanoni, M., 2010. Real time tomography at the swiss light source. AIP Conference Proceedings, 1234, pp. 87–90.

Momose, A., 1995. Demonstration of phase-contrast X-ray computed-tomography using an X-ray interferometer. Nucl. Instrum. Methods Phys. Res., Sect. A 352, 622–628.

Momose, A., Fukuda, J., 1995. Phase-contrast radiographs of nonstained rat cerebellar specimen. Med. Phys. 22, 375–379.

Noda-Saita, K., Yoneyama, A., Shitaka, Y., Hirai, Y., Terai, K., Wu, J., Takeda, T., Hyodo, K., Osakabe, N., Yamaguchi, T., Okada, M., 2006. Quantitative analysis of amyloid plaques in a mouse model of Alzheimer's disease by phase-contrast X-ray computed tomography. Neuroscience 138, 1205–1213.

Nordberg, A., Rinne, J.O., Kadir, A., Långström, B., 2010. The use of PET in Alzheimer disease. Nat. Rev. Neurol. 6, 78–87.

Oakley, H., Cole, S.L., Logan, S., Maus, E., Shao, P., Craft, J., Guillozet-Bongaarts, A., Ohno, M., Disterhoft, J., Van Eldik, L., Berry, R., Vassar, R., 2006. Intraneuronal beta-amyloid aggregates, neurodegeneration, and neuron loss in transgenic mice with five familial Alzheimer's disease mutations: potential factors in amyloid plaque formation. J. Neurosci. 26, 10129–10140.

Paxinos, G., Franklin, K.B.J., 2001. The mouse brain in stereotaxic coordinates, 2nd ed. Academic Press, San Diego.

Petiet, A., Santin, M., Bertrand, A., Wiggins, C.J., Petit, F., Houitte, D., Hantraye, P., Benavides, J., Debeir, T., Rooney, T., Dhenain, M., 2011. Gadolinium-staining reveals amyloid plaques in the brain of Alzheimer's transgenic mice. Neurobiol. Aging http://dx.doi.org/10.1016/j.neurobiolaging.2011.03.009.

Petrella, J.R., Coleman, R.E., Doraiswamy, P.M., 2003. Neuroimaging and early diagnosis of Alzheimer disease: a look to the future. Radiology 226, 315–336.

Pfeiffer, F., David, C., Bunk, O., Donath, T., Bech, M., Le Duc, G., Bravin, A., Cloetens, P., 2008. Region-of-interest tomography for grating-based X-ray differential phase-contrast imaging. Phys. Rev. Lett. 101, 1–4.

Raupach, R., Flohr, T.G., 2011. Analytical evaluation of the signal and noise propagation in x-ray differential phase-contrast computed tomography. Phys. Med. Biol. 56, 2219–2244.

Reitz, C., Brayne, C., Mayeux, R., 2011. Epidemiology of Alzheimer disease. Nat. Rev. Neurol. 7, 137–152.

Revol, V., Kottler, C., Kaufmann, R., Straumann, U., Urban, C., 2010. Noise analysis of grating-based x-ray differential phase contrast imaging. Rev. Sci. Instrum. 81, 073709.

Sage, D., Neumann, F., Hediger, F., Gasser, S., Unser, M., 2005. Automatic tracking of individual fluorescence particles: application to the study of chromosome dynamics. IEEE Trans. Image Process. 14, 1372–1383.

Sorzano, C.O., Thevenaz, P., Unser, M., 2005. Elastic registration of biological images using vector-spline regularization. IEEE Trans. Biomed. Eng. 52, 652–663.

Sperling, R.A., Aisen, P.S., Beckett, L.A., Bennett, D.A., Craft, S., Fagan, A.M., Iwatsubo, T., Jack Jr., C.R., Kaye, J., Montine, T.J., Park, D.C., Reiman, E.M., Rowe, C.C., Siemers, E., Stern, Y., Yaffe, K., Carrillo, M.C., Thies, B., Morrison-Bogorad, M., Wagster, M.V., Phelps, C.H., 2011. Toward defining the preclinical stages of Alzheimer's disease: recommendations from the National Institute on Aging-Alzheimer's Association workgroups on diagnostic guidelines for Alzheimer's disease. Alzheimers Dement. 7, 280–292.

Stampanoni, M., Groso, A., Isenegger, A., Mikuljan, G., Chen, Q., Meister, D., Lange, M., Betemps, R., Henein, S., Abela, R., 2007. TOMCAT: a beamline for tomographic microscopy and coherent radiology experiments. Synchrotron Radiat. Instrum. Pts 1 and 2 879, 848–851.

Thal, D.R., Rub, U., Orantes, M., Braak, H., 2002. Phases of A beta-deposition in the human brain and its relevance for the development of AD. Neurology 58, 1791–1800.

Thevenaz, P., Ruttimann, U., Unser, M., 1998. A pyramid approach to subpixel registration based on intensity. IEEE Trans. Image Process. 7, 27–41.

van Rooden, S., Maat-Schieman, M.L., Nabuurs, R.J., van der Weerd, L., van Duijn, S., van Duinen, S.G., Natte, R., van Buchem, M.A., van der Grond, J., 2009. Cerebral amyloidosis: postmortem detection with human 7.0-T MR imaging system. Radiology 253, 788–796.

Vanhoutte, G., Dewachter, I., Borghgraef, P., Van Leuven, F., Van der Linden, A., 2005. Noninvasive in vivo MRI detection of neuritic plaques associated with iron in APP[V717I] transgenic mice, a model for Alzheimer's disease. Magn. Reson. Med. 53, 607–613.

Wadghiri, Y.Z., Sigurdsson, E.M., Sadowski, M., Elliott, J.I., Li, Y., Scholtzova, H., Tang, C.Y., Aguinaldo, G., Pappolla, M., Duff, K., Wisniewski, T., Turnbull, D.H., 2003.

Detection of Alzheimer's amyloid in transgenic mice using magnetic resonance microimaging. Magn. Reson. Med. 50, 293–302.

Weitkamp, T., Diaz, A., David, C., Pfeiffer, F., Stampanoni, M., Cloetens, P., Ziegler, E., 2005. X-ray phase imaging with a grating interferometer. Opt. Express 13, 6296.

Wengenack, T.M., Reyes, D.A., Curran, G.L., Borowski, B.J., Lin, J., Preboske, G.M., Holasek, S.S., Gilles, E.J., Chamberlain, R., Marjanska, M., Jack Jr., C.R., Garwood, M., Poduslo, J.F., 2011. Regional differences in MRI detection of amyloid plaques in AD transgenic mouse brain. Neuroimage 54, 113–122.

Wisniewski, H.M., Bancher, C., Barcikowska, M., Wen, G.Y., Currie, J., 1989. Spectrum of morphological appearance of amyloid deposits in Alzheimer's disease. Acta Neuropathol. 78, 337–347.

Yang, J., Wadghiri, Y.Z., Hoang, D.M., Tsui, W., Sun, Y., Chung, E., Li, Y., Wang, A., de Leon, M., Wisniewski, T., 2011. Detection of amyloid plaques targeted by USPIO-Abeta1-42 in Alzheimer's disease transgenic mice using magnetic resonance microimaging. Neuroimage 55, 1600–1609.

Zhang, J., Yarowsky, P., Gordon, M.N., Di Carlo, G., Munireddy, S., van Zijl, P.C., Mori, S., 2004. Detection of amyloid plaques in mouse models of Alzheimer's disease by magnetic resonance imaging. Magn. Reson. Med. 51, 452–457.

Zhou, S.A., Brahme, A., 2008. Development of phase-contrast X-ray imaging techniques and potential medical applications. Phys. Med. 24, 129–148.

Zhu, P., Zhang, K., Wang, Z., Liu, Y., Liu, X., Wu, Z., McDonald, S.A., Marone, F., Stampanoni, M., 2010. Low-dose, simple, and fast grating-based X-ray phase-contrast imaging. Proc. Natl. Acad. Sci. U. S. A. 107, 13576–13581.